Eidgenössische Technische Hochschule Zürich

Ecole polytechnique fédérale de Zurich
Politecnico federale di Zurigo
Swiss Federal Institute of Technology Zurich

Computation of Resonant Modes for Axisymmetric Cavities using *hp*-Version Finite Elements

R. Hiptmair and P.D. Ledger

Research Report No. 2003-15
November 2003

Seminar für Angewandte Mathematik
Eidgenössische Technische Hochschule
CH-8092 Zürich
Switzerland

Computation of Resonant Modes for Axisymmetric Cavities using *hp*-Version Finite Elements

R. Hiptmair and P.D. Ledger

Seminar für Angewandte Mathematik
Eidgenössische Technische Hochschule
CH-8092 Zürich
Switzerland

Research Report No. 2003-15 November 2003

Abstract

The computation of the resonant frequencies for open and closed cavities is not a trivial task: Multi–materials and sharp corners all give rise to highly singular eigenfunctions. However, an approach using *hp*–finite elements is well suited to such problems and, with the correct combination of *h*– and *p*–refinements, it yields the theoretically predicated exponential rates of convergence.

In this paper, we present a novel approach to the solution of axisymmetric cavity problems which uses a hierarchic H^1 and $\vec{H}(\mathrm{curl})$ conforming finite element basis. A selection of numerical examples are included and these demonstrate that the exponential rates of convergence are achieved in practice.

1 Introduction

Our interest in this paper lies in the accurate evaluation of Maxwell eigenvalues for open and closed cavity problems. The results are important for many applications such as the design of Microwave devices and charged particle accelerators. However, the solution of these problems is far from being a trivial task as realistic cavities often contain multi-materials, have small scale features and contain many sharp corners all giving rise to highly singular eigenfunctions.

It is well known that the application of standard nodal finite elements to the solution of Maxwell cavity problems is inappropriate as the resulting solution is polluted by so-called spurious modes which relate to non-physical solutions [30, 21]. To overcome this problem, there has been much interest in the application of $\boldsymbol{H}(\mathrm{curl})$ conforming applications first introduced by Nédélec [22, 23, 24]. These are known to eliminate the problems of spurious modes and allow easy incorporation of material interfaces and boundary conditions. Amongst the engineering community these elements are better known as edge elements, as in the case of the lowest order element, there is a degree of freedom associated with each edge of the element. Over the last two decades there has been a tremendous number of different $\boldsymbol{H}(\mathrm{curl})$ conforming elements proposed, for both two– and three–dimensions e.g. [32, 14, 6, 17, 27, 32] . For a review of recent developments in two–dimensional edge elements we refer to [2], whilst for a summary of three-dimensional developments we refer to [3]. Of particular relevance to this work, are approaches which allow an arbitrary increase in the polynomial order. Demkowicz and coworkers [12, 13] have development a two–dimensional hybrid triangular/quadrilateral element package which allows for hp–refinement. More recently, Ainsworth and Coyle have proposed an alternative hybrid discretisation with better conditioning properties [2]. In three-dimensions, an approach employing anisotropic refinements and hierarchic hexahedral elements has been proposed by Rachowicz and Demkowicz [26]. An alternative strategy, which uses hierarchic tetrahedral elements has been proposed by Ainsworth and Coyle [3].

Ainsworth and Coyle [1] demonstrate that using the appropriate combinations of h– and p–refinement, results in an exponential rate of convergence for the computed eigenvalues of a sequence of challenging benchmark problems in two–dimensions. In related work, exponential rates of convergence were demonstrated for the eigenvalues of a straight sided three-dimensional cavity problem when a hierarchic tetrahedral discretisation was employed [4]. Furthermore, for three-dimensional cavities with curved boundaries, exponential rates of convergence for the Maxwell eigenvalues have also been observed [11].

In this work, we consider a special class of three-dimensional problems, which, through rotational symmetry, allows their reduction to a sequence of two–dimensional problems. This class of problems is of great interest, as it enables the solution of complete three–dimensional problems with much reduced computational effort. Previous investigations of these axisymmetric eigenvalue problems have employed only first or second order elements [16, 33, 15, 20, 25, 9, 8]. Of particular importance is the recent work by Chinellato *et al.* [9, 8] who demonstrated the superiority of using second order elements over an approach using first order elements. In this work, we show a novel approach to this problem which employs the two–dimensional hierarchical $\boldsymbol{H}(\mathrm{curl})$ and H^1 conforming discretisations of Ainsworth and Coyle, thus allowing for an arbitrary increase in polynomial order.

When one's interest lies in the simulation of open cavities then one must also approximate the infinite region of free space which surrounds the cavity. A suitable approach for doing this must be found. Perfectly matched layers (PML's) were introduced by Berenger [7] as a means of truncating the infinite free space domain which occurs when performing electromagnetic scattering problems with time domain finite difference methods. The use of PML's has since been extended to include electromagnetic scattering simulations by finite element methods, both in the time and frequency domain. For example, in [19] a PML was successfully used in conjunction with hierarchic $\boldsymbol{H}(\mathrm{curl})$ conforming basis for the solution of electromagnetic scattering problems. Whilst, in recent work by Streiff Witzig and Fichtner [28] a PML was used to simulate open cavity problems. These problems are particularly challenging for absorbing boundary conditions as the frequency of the wave to be absorbed is not known a priori. In view of this and following our previous success with scattering simulations we adopt the PML for the truncations of domains which involve open cavity

resonators.

The presentation of the work proceeds as follows: In Section 2 we present the problem formulation for the axisymmetric eigenvalue problem. Then, in Section 3 we give an overview of Ainsworth and Coyle's hierarchic $\boldsymbol{H}(\mathrm{curl})$ and H^1 conforming basis functions. Issues related to the computational procedure are discussed in Section 4. Whilst Section 5 describes a series of numerical examples which demonstrate the performance of the proposed procedure. The article closes with some concluding remarks.

2 Problem formulation

Let us first consider the Maxwell eigenvalue problem that is set in the bounded domain $\Omega \subset \mathbb{R}^3$ which involves identifying the non-trivial electric field $\boldsymbol{E}$ and the corresponding resonant frequencies $\omega \in \mathbb{C} \setminus \{0\}$ that satisfy

$$\begin{aligned} \mathrm{curl}\left(\mu^{-1}\mathrm{curl}\,\boldsymbol{E}\right) - \omega^2\epsilon\boldsymbol{E} &= \boldsymbol{0} \qquad \text{in } \Omega & (1)\\ \boldsymbol{n}\wedge\boldsymbol{E} &= \boldsymbol{0} \qquad \text{on } \partial\Omega & (2)\end{aligned}$$

where (1) is the vector–wave equation and $\boldsymbol{n}$ is the outward unit normal to $\partial\Omega$. The permeability μ and the permitivity ϵ, which may be complex valued, are determined by the material properties of Ω. Standard variational arguments incorporating (1) and (2) require that we seek $\boldsymbol{E} \in \boldsymbol{H}_0^{(3)}(\mathrm{curl};\Omega)$ and $\omega \in \mathbb{C} \setminus \{0\}$ such that

$$(\mu^{-1}\mathrm{curl}\,\boldsymbol{E}, \mathrm{curl}\,\boldsymbol{F})_\Omega - \omega^2\,(\epsilon\boldsymbol{E}, \boldsymbol{F})_\Omega = 0 \tag{3}$$

for every $\boldsymbol{F} \in \boldsymbol{H}_0^{(3)}(\mathrm{curl};\Omega)$ where

$$\boldsymbol{H}^{(3)}(\mathrm{curl};\Omega) = \left\{\boldsymbol{u} \in (L_2(\Omega))^3,\, \mathrm{curl}\,\boldsymbol{u} \in (L_2(\Omega))^3\right\}$$

$$\boldsymbol{H}_0^{(3)}(\mathrm{curl};\Omega) = \{\boldsymbol{u} \in \boldsymbol{H}(\mathrm{curl};\Omega),\, \boldsymbol{n}\wedge\boldsymbol{u} = \boldsymbol{0} \text{ on } \partial\Omega\}$$

and $(\cdot,\cdot)_\Omega$ is the usual L_2 inner product over Ω. For the discrete solution, a proof exists which show that a finite element discretisation of equation (3) which uses only the lowest order $\boldsymbol{H}^{(3)}(\mathrm{curl};\Omega)$ conforming elements, leads to a spurious free solution. The proof is not yet available for higher order $\boldsymbol{H}^{(3)}(\mathrm{curl};\Omega)$ conforming approximations, although numerical experiments confirm that spurious modes are not produced in this case either.

2.1 Axisymmetric problems

We now restrict consideration to problems which are axisymmetric. The derivation of the weak variational statement has already been extensively described in previous works [16, 33, 15, 20, 25, 9, 8], and so we summarise only the key elements. Firstly, we introduce the set of cylindrical coordinates so that the electric field in cylindrical coordinates $\tilde{\boldsymbol{E}}$ has components $\tilde{E}_r, \tilde{E}_\theta$ and $\tilde{E}_z$. The benefits of this approach become clear when it is assumed that the material tensors ϵ and μ have no variation in the θ direction. A Fourier series expansion of the field is performed, so that

$$\tilde{\boldsymbol{E}} = \sum_{m=0}^{\infty} \tilde{\boldsymbol{E}}_m^{(c)} \cos(m\theta) + \tilde{\boldsymbol{E}}_m^{(s)} \sin(m\theta) \tag{4}$$

where $\tilde{\boldsymbol{E}}_m^{(c)} = [E_{m,r}^{(c)}, E_{m,\theta}^{(c)}, E_{m,z}^{(c)}]^T$ and $\tilde{\boldsymbol{E}}_m^{(s)} = [E_{m,r}^{(s)}, E_{m,\theta}^{(s)}, E_{m,z}^{(s)}]^T$ are functions only of r and z. It is beneficial to introduce the notation $\tilde{\boldsymbol{E}}_{m,p}^{(c)} = [\tilde{E}_{m,r}^{(c)}, \tilde{E}_{m,z}^{(c)}]^T$ and $\tilde{\boldsymbol{E}}_{m,p}^{(s)} = [\tilde{E}_{m,r}^{(s)}, \tilde{E}_{m,z}^{(s)}]^T$ to describe the in–plane components of $\tilde{\boldsymbol{E}}_m^{(c)}$ and $\tilde{\boldsymbol{E}}_m^{(s)}$, respectively. Applying these definitions to the variational statement given in equation (3), together with the appropriate definition of the curl in cylindrical coordinates, leads to a sequence of two–dimensional eigenvalue problems. In the following the subscript m has been omitted to improve the clarity of the presentation.

The first problem states that, for a given angular wave number m, find $\tilde{\boldsymbol{E}}_p^{(c)} \in \boldsymbol{H}_0^{(2)}(\mathrm{curl};\Omega)$ and $\tilde{E}_\theta^{(s)} \in H_0^1$ such that

$$\begin{aligned}(\mu_\theta^{-1} r \,\mathrm{curl}_p\, \tilde{\boldsymbol{E}}_p^{(c)}, \mathrm{curl}_p\, \tilde{\boldsymbol{F}}_p)_\Omega + (\mu_p^{-1} r^{-1}\, \nabla_p(r\tilde{E}_\theta^{(s)}), \nabla_p(r\tilde{F}_\theta))_\Omega + m^2(\mu_p^{-1} r^{-1}\, \tilde{\boldsymbol{E}}_p^{(c)}, \tilde{\boldsymbol{F}}_p)_\Omega + \\ + m(\mu_p^{-1} r^{-1}\, \nabla_p(r\tilde{E}_\theta^{(s)}), \tilde{\boldsymbol{F}}_p)_\Omega + m(\mu_p^{-1}\, \tilde{\boldsymbol{E}}_p^{(c)}, r^{-1}\, \nabla_p(r\tilde{F}_\theta))_\Omega = \\ = \omega^2(\epsilon_p r\, \tilde{\boldsymbol{E}}_p^{(c)}, \tilde{\boldsymbol{F}}_p)_\Omega + \omega^2(\epsilon_\theta r\, \tilde{E}_\theta^{(c)}, \tilde{F}_\theta)_\Omega \end{aligned} \tag{5}$$

for all $\boldsymbol{F}_p \in \boldsymbol{H}_0^{(2)}(\mathrm{curl};\Omega)$ and $\tilde{F}_\theta \in H_0^1$. The second problem is find $\tilde{\boldsymbol{E}}_p^{(s)} \in \boldsymbol{H}_0^{(2)}(\mathrm{curl};\Omega)$ and $\tilde{E}_\theta^{(c)} \in H_0^1$ such that

$$\begin{aligned}(\mu_\theta^{-1} r \,\mathrm{curl}_p\, \tilde{\boldsymbol{E}}_p^{(s)}, \mathrm{curl}_p\, \tilde{\boldsymbol{F}}_p)_\Omega + (\mu_p^{-1} r^{-1}\, \nabla_p(r\tilde{E}_\theta^{(c)}), \nabla_p(r\tilde{F}_\theta))_\Omega + m^2(\mu_p^{-1} r^{-1}\, \tilde{\boldsymbol{E}}_p^{(s)}, \tilde{\boldsymbol{F}}_p)_\Omega - \\ - m(\mu_p^{-1} r^{-1}\, \nabla_p(r\tilde{E}_\theta^{(c)}), \tilde{\boldsymbol{F}}_p)_\Omega - m(\mu_p^{-1}\, \tilde{\boldsymbol{E}}_p^{(s)}, r^{-1}\, \nabla_p(r\tilde{F}_\theta))_\Omega = \\ = \omega^2(\epsilon_p r\, \tilde{\boldsymbol{E}}_p^{(s)}, \tilde{\boldsymbol{F}}_p)_\Omega + \omega^2(\epsilon_\theta r\, \tilde{E}_\theta^{(c)}, \tilde{F}_\theta)_\Omega \end{aligned} \tag{6}$$

for all $\boldsymbol{F}_p \in \boldsymbol{H}_0^{(2)}(\mathrm{curl};\Omega)$ and $\tilde{F}_\theta \in H_0^1$. In the above, the subscript p on gradient and curl operations refers to differentiation with respect to the in-plane components (r, z).

The space $\boldsymbol{H}_0^{(2)}(\mathrm{curl};\Omega)$ introduced above is defined as

$$\boldsymbol{H}_0^{(2)}(\mathrm{curl};\Omega) = \left\{ \boldsymbol{u} \in \boldsymbol{H}^{(2)}(\mathrm{curl};\Omega), \boldsymbol{n} \wedge \boldsymbol{u} = \boldsymbol{0} \text{ on} \partial\Omega \right\}$$

where

$$\boldsymbol{H}^{(2)}(\mathrm{curl};\Omega) = \left\{ \boldsymbol{u} \in (L_2(\Omega))^2,\, \mathrm{curl}_p\, \boldsymbol{u} \in (L_2(\Omega)) \right\}$$

Note that the second weak variational statement may be obtained from the first by a simple change of variables, ie. $\tilde{\boldsymbol{E}}_p^{(s)} = \tilde{\boldsymbol{E}}_p^{(c)}$ and $\tilde{E}_\theta^{(c)} = -\tilde{E}_\theta^{(s)}$. Therefore it suffices to consider the solution of only one of the two given variational statements, of which we choose the first.

2.2 Application of boundary conditions at the radial axis

There has been much discussion about the appropriate boundary conditions that should be imposed on the radial axis $r = 0$ [16, 33, 15, 20, 25, 9, 8]. These are usually performed on a discrete level, and often lead to conditions which are difficult to impose and unnatural to the finite element approach.

In this work, we propose an alternative strategy for obtaining boundary conditions which is performed on the continuous level. Consider the evaluation of the $\boldsymbol{H}^{(2)}(\mathrm{curl};\Omega)$ norm

$$\|\tilde{\boldsymbol{E}}\|^2 = \int_z \int_r \int_0^{2\pi} |\tilde{\boldsymbol{E}}|^2 + |\mathrm{curl}\, \tilde{\boldsymbol{E}}|^2 \, r \mathrm{d}\theta \mathrm{d}r \mathrm{d}z \tag{7}$$

for the case of angular wave number $m = 1$, which can be expressed as

$$\|\tilde{\boldsymbol{E}}\|^2 = \pi \int_z \int_r \frac{1}{r}\tilde{E}_z^2 + r\left(\frac{\partial \tilde{E}_\theta}{\partial z}\right)^2 + r\left(\frac{\partial \tilde{E}_r}{\partial z} - \frac{\partial \tilde{E}_r}{\partial r}\right)^2 + \frac{1}{r}\left(\frac{\partial}{\partial r}(r\tilde{E}_\theta)\right)^2 + r(2\tilde{E}_r^2 + \tilde{E}_\theta^2 + \tilde{E}_z^2)\mathrm{d}r\mathrm{d}z \tag{8}$$

We require that all terms which involve $1/r$ must tend to zero at the radial axis $r = 0$. In numerical experiments it has been observed that if numerical quadrature of sufficient degree is employed for evaluating the integrals then bounded-ness of the integrands can be achieved without employing any special conditions. We hope to give a full theoretical justification of this in future work.

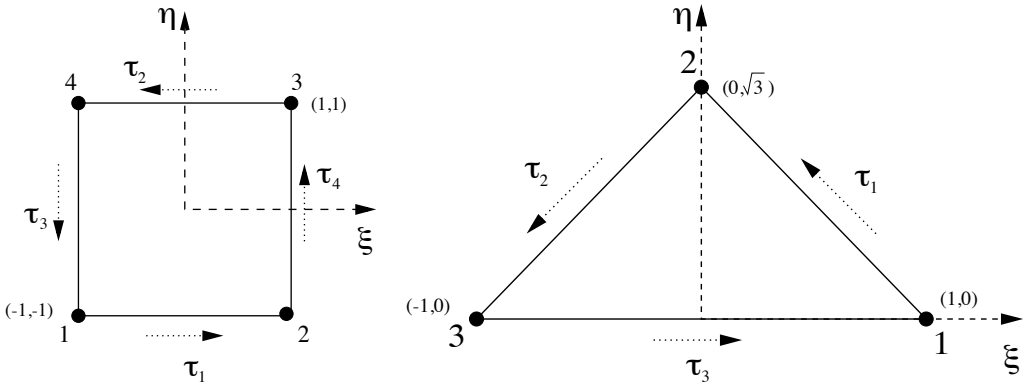

Quadilateral Reference Element Triangular Reference Element

Figure 1: Reference elements used in Ainsworth and Coyle's [2] hierarchic basis

Entity	Quadrilateral	Triangle
Vertices	$\hat{\psi}_1 = \frac{1}{4}(1-\xi)(1-\eta)$ $\hat{\psi}_2 = \frac{1}{4}(1+\xi)(1-\eta)$ $\hat{\psi}_3 = \frac{1}{4}(1+\xi)(1+\eta)$ $\hat{\psi}_4 = \frac{1}{4}(1-\xi)(1+\eta)$	$\hat{\psi}_1 = \hat{\lambda}_1 = \frac{1}{2\sqrt{3}}(\sqrt{3}+\sqrt{3}\xi-\eta)$ $\hat{\psi}_2 = \hat{\lambda}_2 = \frac{\eta}{\sqrt{3}}$ $\hat{\psi}_3 = \hat{\lambda}_3 = \frac{1}{2\sqrt{3}}(\sqrt{3}-\sqrt{3}\xi-\eta)$
Edges	$\hat{\psi}_1^j = \frac{1}{2}\ell_j(\xi)(1-\eta)$ $\hat{\psi}_2^j = \frac{1}{2}\ell_j(-\xi)(1+\eta)$ $j=2,\cdots,p$ $\hat{\psi}_3^j = \frac{1}{2}\ell_j(-\eta)(1-\xi)$ $\hat{\psi}_4^j = \frac{1}{2}\ell_j(\eta)(1+\xi)$	$\hat{\psi}_1^j = \hat{\lambda}_1\hat{\lambda}_2\varphi_{j-2}(\hat{\lambda}_2-\hat{\lambda}_1)$ $\hat{\psi}_2^j = \hat{\lambda}_2\hat{\lambda}_3\varphi_{j-2}(\hat{\lambda}_3-\hat{\lambda}_2)$ $j=2,\cdots,p$ $\hat{\psi}_3^j = \hat{\lambda}_3\hat{\lambda}_1\varphi_{j-2}(\hat{\lambda}_1-\hat{\lambda}_3)$
Interiors	$\hat{\psi}_{j,k}^I = \ell_j(\xi)\ell_k(\eta)\ j,k = 2\cdots p$	$\hat{\psi}_{j,k}^I = \hat{\lambda}_1\hat{\lambda}_2\hat{\lambda}_3 L_j(\hat{\lambda}_1-\hat{\lambda}_3)L_k(2\hat{\lambda}_2-1)$ $0 \le j,k,j+k \le p-3$

Table 1: Ainsworth and Coyle's [2] hierarchic H^1 conforming basis functions.

3 Hierarchic discretisation

In this section we provide a brief summary of Ainsworth and Coyle's [2] hierarchic basis functions which will be used to provide a discrete approximation to the continuous functional spaces $\boldsymbol{H}^{(2)}(\mathrm{curl};\Omega)$ and $H^1(\Omega)$.

First, let us consider the basis functions for H^1. It turns out that these can be decomposed in to functions associated with the vertices, edges and interior of the element. We follow Ainsworth and Coyle and introduce the reference square $[-1,1]^2$ and the reference triangle with vertices $(1,0)$, $(0,\sqrt{3})$ and $(-1,0)$, as illustrated in Figure 1. On each of the two diagrams shown in this figure, the numbering given relates to vertex and edge numbers. The hierarchic basis functions for the triangles and quadrilaterals is shown in Table 1. In this table ℓ_j is the integrated Legendre polynomial of degree j, L_j is the Legendre polynomial of degree j and the polynomial φ_j is defined as

$$\varphi_j(s) = \frac{-4}{(j+2)(j+1)} L_j(s) \tag{9}$$

This polynomial is introduced to ensure compatibility of the edge basis functions on edges between neighbouring triangular and quadrilateral elements.

In Table 2 we present Ainsworth and Coyle's $\boldsymbol{H}^{(2)}(\mathrm{curl};\Omega)$ conforming hierarchic basis functions. These functions reside on the edges and the interiors of the quadrilateral and triangular elements. For these basis functions the Jacobi polynomials $P_j^{\alpha,\beta}$ of degree j are also required.

Entity	Quadrilateral	Triangle
Edges ($p=0$)	$\hat{\boldsymbol{\phi}}_1^0 = \frac{1}{2}(1-\eta)\begin{pmatrix}1\\0\end{pmatrix}$ $\hat{\boldsymbol{\phi}}_2^0 = \frac{1}{2}(1+\eta)\begin{pmatrix}-1\\0\end{pmatrix}$ $\hat{\boldsymbol{\phi}}_3^0 = \frac{1}{2}(1-\xi)\begin{pmatrix}0\\-1\end{pmatrix}$ $\hat{\boldsymbol{\phi}}_4^0 = \frac{1}{2}(1+\xi)\begin{pmatrix}0\\1\end{pmatrix}$	$\hat{\boldsymbol{\phi}}_1^0 = \hat{\lambda}_1\hat{\nabla}\hat{\lambda}_2 - \hat{\lambda}_2\hat{\nabla}\hat{\lambda}_1$ $\hat{\boldsymbol{\phi}}_1^0 = \hat{\lambda}_2\hat{\nabla}\hat{\lambda}_3 - \hat{\lambda}_3\hat{\nabla}\hat{\lambda}_2$ $\hat{\boldsymbol{\phi}}_1^0 = \hat{\lambda}_3\hat{\nabla}\hat{\lambda}_1 - \hat{\lambda}_1\hat{\nabla}\hat{\lambda}_3$
Edges ($p=1$)	$\hat{\boldsymbol{\phi}}_1^1 = \frac{1}{2}(1-\eta)L_1(\xi)\begin{pmatrix}1\\0\end{pmatrix}$ $\hat{\boldsymbol{\phi}}_2^1 = \frac{1}{2}(1+\eta)L_1(-\xi)\begin{pmatrix}-1\\0\end{pmatrix}$ $\hat{\boldsymbol{\phi}}_3^1 = \frac{1}{2}(1-\xi)L_1(-\eta)\begin{pmatrix}0\\-1\end{pmatrix}$ $\hat{\boldsymbol{\phi}}_4^1 = \frac{1}{2}(1+\xi)L_1(\eta)\begin{pmatrix}0\\1\end{pmatrix}$	$\hat{\boldsymbol{\phi}}_1^1 = \hat{\lambda}_1\hat{\nabla}\hat{\lambda}_2 + \hat{\lambda}_2\hat{\nabla}\hat{\lambda}_1$ $\hat{\boldsymbol{\phi}}_1^1 = \hat{\lambda}_2\hat{\nabla}\hat{\lambda}_3 + \hat{\lambda}_3\hat{\nabla}\hat{\lambda}_2$ $\hat{\boldsymbol{\phi}}_1^1 = \hat{\lambda}_3\hat{\nabla}\hat{\lambda}_1 + \hat{\lambda}_1\hat{\nabla}\hat{\lambda}_3$
Edges ($p\geq 2$)	$\hat{\boldsymbol{\phi}}_1^j = \frac{1}{2}(1-\eta)L_j(\xi)\begin{pmatrix}1\\0\end{pmatrix}$ $\hat{\boldsymbol{\phi}}_2^j = \frac{1}{2}(1+\eta)L_j(-\xi)\begin{pmatrix}-1\\0\end{pmatrix}$ $\hat{\boldsymbol{\phi}}_3^j = \frac{1}{2}(1-\xi)L_j(-\eta)\begin{pmatrix}0\\-1\end{pmatrix}$ $\hat{\boldsymbol{\phi}}_4^j = \frac{1}{2}(1+\xi)L_j(\eta)\begin{pmatrix}0\\1\end{pmatrix}$ $j=2,\cdots,p$	$\hat{\boldsymbol{\phi}}_1^j = \frac{1-2j}{j}L_{j-1}(\hat{\lambda}_2-\hat{\lambda}_1)\hat{\boldsymbol{\phi}}_1^1 - \frac{j-1}{j}L_{j-2}(\hat{\lambda}_2-\hat{\lambda}_1)\boldsymbol{\phi}_1^0$ $\hat{\boldsymbol{\phi}}_2^j = \frac{1-2j}{j}L_{j-1}(\hat{\lambda}_3-\hat{\lambda}_2)\hat{\boldsymbol{\phi}}_2^1 - \frac{j-1}{j}L_{j-2}(\hat{\lambda}_3-\hat{\lambda}_2)\boldsymbol{\phi}_2^0$ $\hat{\boldsymbol{\phi}}_3^j = \frac{1-2j}{j}L_{j-1}(\hat{\lambda}_1-\hat{\lambda}_3)\hat{\boldsymbol{\phi}}_3^1 - \frac{j-1}{j}L_{j-2}(\hat{\lambda}_1-\hat{\lambda}_3)\boldsymbol{\phi}_3^0$ $j=2,\cdots,p$
Interiors	$\hat{\boldsymbol{\phi}}_{j,k}^{I\xi} = L_j(\xi)\ell_k(\eta)\begin{pmatrix}1\\0\end{pmatrix}$ $\hat{\boldsymbol{\phi}}_{j,k}^{I\eta} = L_j(\eta)\ell_k(\xi)\begin{pmatrix}0\\1\end{pmatrix}$ $j=0,\cdots,p$ $k=2,\cdots,p+1$	$\hat{\boldsymbol{\phi}}_{1,j}^{PI} = \hat{\lambda}_1\hat{\lambda}_2\hat{\nabla}\hat{\lambda}_3 L_j(\hat{\lambda}_2-\hat{\lambda}_1)$ $\hat{\boldsymbol{\phi}}_{2,j}^{PI} = \hat{\lambda}_2\hat{\lambda}_3\hat{\nabla}\hat{\lambda}_1 L_j(\hat{\lambda}_3-\hat{\lambda}_2)$ $\hat{\boldsymbol{\phi}}_{3,j}^{PI} = \hat{\lambda}_3\hat{\lambda}_1\hat{\nabla}\hat{\lambda}_2 L_j(\hat{\lambda}_1-\hat{\lambda}_3)$ $j=0,\cdots,p-2$ $\hat{\boldsymbol{\phi}}_{j,k}^{GI\xi} = \hat{\lambda}_1\hat{\lambda}_2\hat{\lambda}_3(1-\hat{\lambda}_1)^j P_j^{2,2}\left(\frac{\hat{\lambda}_1-\hat{\lambda}_3}{1-\hat{\lambda}_2}\right)P_k^{2j+5,2}(2\hat{\lambda}_2-1)\begin{pmatrix}1\\0\end{pmatrix}$ $\hat{\boldsymbol{\phi}}_{j,k}^{GI\eta} = \hat{\lambda}_1\hat{\lambda}_2\hat{\lambda}_3(1-\hat{\lambda}_1)^j P_j^{2,2}\left(\frac{\hat{\lambda}_1-\hat{\lambda}_3}{1-\hat{\lambda}_2}\right)P_k^{2j+5,2}(2\hat{\lambda}_2-1)\begin{pmatrix}0\\1\end{pmatrix}$ $0\leq j, kj+k\leq p-3$

Table 2: Ainsworth and Coyle's [2] hierarchic $\boldsymbol{H}^{(2)}(\mathrm{curl};\Omega)$ conforming basis functions.

4 Computational procedure

The variational statement given in equation (5) is discretised using the basis functions given in Section 3. Specifically, $\tilde{\boldsymbol{E}}_p^{(c)}$ is discretised by the $\boldsymbol{H}^{(2)}(\mathrm{curl};\Omega)$ conforming basis and $\tilde{E}_\theta^{(s)}$ by the H^1 basis multiplied by $1/r$. This choice is made so that the gradients of the H^1 basis lie in the space of the $\boldsymbol{H}^{(2)}(\mathrm{curl};\Omega)$ conforming elements.

Integrals are evaluated by employing Gauss numerical quadrature points residing only in the interior of the triangular and quadrilateral elements. Elements which lie next to the $r = 0$ radius axis have singular terms in the integrands. To ensure that these are resolved with sufficient accuracy a Gauss integration scheme with at least $3(p+1)$ points in the radial direction has been implemented for quadrilateral elements. As a numerical justification of this we consider the accuracy of the first eigenvalue of a hollow cylindrical cavity when a discretisation consisting of a single quadrilateral element is used in conjunction with polynomial orders $p = 0, 1, 2, 3, 4, 5$ in turn. For each case Gauss integration schemes with $p+1, 2(p+1), 3(p+1)$ and $4(p+1)$ points in the radial direction are considered. A description of this problem appears later in this article, here, it suffices to say that the example has an exact solution so that the relative errors may be computed. The results of this investigation are shown in Figure 2. In this figure it is observed that when at least $3(p+1)$ integration points are used in the radial direction the relative error reaches a plateau for which further increases in the number of integration points do not effect the relative error obtained. For the case of $p = 5$, the precision limit is reached and hence the plateau is not clearly displayed.

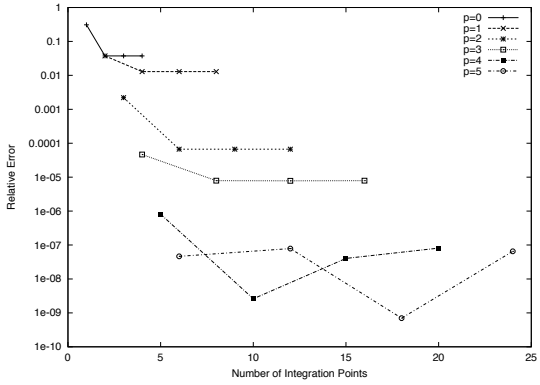

Figure 2: Axisymmetric eigenvalue calculations for a hollow cylindrical cavity of unit height and radius showing, the convergence of the relative error against number of integration points for the first eigenvalue of the case of angular wavenumber $m = 0$ on a single quadrilateral meshes with uniform polynomial orders $p = 0, 1, 2, 3, 4, 5$ in turn.

When integrating in the non radial direction on quadrilateral elements, one can employ the standard rule that an n point Gauss quadrature formula integrates a polynomial of degree $2n - 1$, exactly. For the triangular elements, we employ a Gauss integration scheme with $(3p + 1)^2$ points [29].

To map a vector valued $\boldsymbol{H}^{(2)}(\mathrm{curl};\Omega)$ conforming basis function $\hat{\boldsymbol{\phi}}$ defined on the reference element to a vector valued function $\boldsymbol{\phi}$ defined on a general, possibly curved, element, a covariant projection is employed. When curved boundaries are employed, an exact representation is achieved using the linear blending function approach [31, 18]. With curved boundaries increased numbers of integration points, depending on the curvature of the edges of the element, are used.

Standard continuity requirements are enforced between elements for the H^1 and $\boldsymbol{H}^{(2)}(\mathrm{curl};\Omega)$ conforming elements. This results in application of tangential continuity of the edge basis functions between neighbouring elements for the $\boldsymbol{H}^{(2)}(\mathrm{curl};\Omega)$ space, and continuity of the vertex and edge basis functions between neighbouring elements for the H^1 space. Finally, after application of

boundary conditions, one arrives at the matrix eigenvalue problem

$$\begin{bmatrix} \boldsymbol{K}^{pp} & \boldsymbol{K}^{p\theta} \\ \boldsymbol{K}^{p\theta T} & \boldsymbol{K}^{\theta\theta} \end{bmatrix} \begin{bmatrix} \hat{\tilde{\boldsymbol{E}}}_p \\ \hat{\tilde{\boldsymbol{E}}}_\theta \end{bmatrix} = \omega^2 \begin{bmatrix} \boldsymbol{M}^{pp} & 0 \\ 0 & \boldsymbol{M}^{\theta\theta} \end{bmatrix} \begin{bmatrix} \hat{\tilde{\boldsymbol{E}}}_p \\ \hat{\tilde{\boldsymbol{E}}}_\theta \end{bmatrix} \tag{10}$$

with typical entries

$$\boldsymbol{K}^{pp}_{ij} = \int_\Omega \mu_\theta^{-1} r \mathrm{curl}_p\, \boldsymbol{\phi}_i \cdot \mathrm{curl}_p\, \boldsymbol{\phi}_j \,\mathrm{d}\Omega + m^2 \int_\Omega \mu_p^{-1} r^{-1} \boldsymbol{\phi}_i \cdot \boldsymbol{\phi}_j \mathrm{d}\Omega \tag{11}$$

$$\boldsymbol{K}^{p\theta}_{ij} = m \int_\Omega \mu_p^{-1} r^{-1} \boldsymbol{\phi}_i \cdot \nabla_p \psi_j \mathrm{d}\Omega \tag{12}$$

$$\boldsymbol{K}^{\theta\theta}_{ij} = \int_\Omega \mu_p^{-1} r^{-1} \nabla_p \psi_i \cdot \nabla_p \psi_j \mathrm{d}\Omega \tag{13}$$

$$\boldsymbol{M}^{pp}_{ij} = \int_\Omega \epsilon_p r \boldsymbol{\phi}_i \cdot \boldsymbol{\phi}_j \mathrm{d}\Omega \tag{14}$$

$$\boldsymbol{M}^{\theta\theta}_{ij} = \int_\Omega \epsilon_\theta r^{-1} \psi_i \cdot \psi_j \mathrm{d}\Omega \tag{15}$$

Note that the entries in the vectors $\hat{\tilde{\boldsymbol{E}}}_p$ and $\hat{\tilde{\boldsymbol{E}}}_\theta$ correspond to the unknown coefficients, which when combined with a linear combination of the basis functions provides an approximation of $\tilde{\boldsymbol{E}}_p^{(c)}$ and $\tilde{E}_\theta^{(s)}$, respectively. Henceforth we shall denote $\lambda = \omega^2$ as the eigenvalues of this eigenvalue problem. A numerical solution to this eigenvalue problem is computed using the FORTRAN subroutine set EISPACK of LAPACK.

5 Numerical examples

In this section we present a series of numerical examples which demonstrate the computational performance of the proposed procedure. A series of challenging test cases were proposed by Chinellato *et al.* [9] for testing their computational approach. In this work, we repeat these benchmark calculations and report our findings for the *hp*–finite element approach described above.

The first benchmark consists of determining the resonant modes for a hollow cylindrical cavity whose contents are empty and walls assumed to be PEC's. Next, an example consisting of two concentric spheres with differing material properties is considered. The third and final benchmark is that of a dielectric sphere situated in free space. This is a particular challenging example as one is required to simulate the infinite region of free space surrounding the sphere.

5.1 A hollow cylindrical cavity

This cavity is assumed to be empty so that $\epsilon = \mu = \boldsymbol{I}$ are the identity tensor and the cavity is assumed to have PEC walls. The height and radius of the cavity are assumed to be of unit length. The eigenmodes of this cavity have an analytical solution and their values can be found in [9].

We first consider a discretisation employing quadrilateral elements. Meshes with uniform spacing and containing 1,4,16 and 64 elements were generated, illustrations of these meshes can be found in Figure 3. Initially we consider the case of angular wavenumber $m = 0$. On each of these meshes, computations employing uniform polynomial orders of $p = 0, 1, 2, 3, 4, 5$ were considered in turn, and eigenvalues were computed. In Figure 4, we show the convergence of the first three eigenvalues. Each curve represents a mesh, and the points along the curves represent increasing polynomial order. For each eigenvalue, we show the convergence of the relative error with respect to number of degrees of freedom (Ndof) and with respect to $(\mathrm{Ndof})^{1/2}$.

In previous two–dimensional studies, it was observed that the convergence of eigenvalues was exponential with respect to $(\mathrm{Ndof})^{1/2}$ when the solution is analytic, i.e.

$$|\tilde{\lambda}_i - \lambda_i|/\lambda_i \leq C \exp\{-\alpha \mathrm{Ndof}^{1/2}\} \tag{16}$$

where C and α are constants. This was further confirmed by theoretical investigations by Ainsworth and Pinchedez [5], under certain assumptions about the regularity of the solution. We plot the logarithm relative error against $(\text{Ndof})^{1/2}$ as we believe that the error should converge exponentially fast with increasing p on each of the meshes.

But first, let us consider the convergence of the error with respect to Ndof. For the first eigenvalue, we observe that increasing the polynomial order on the coarsest mesh leads to a fast convergence of the error. We observe that the convergence behaviour for the other meshes is similar so that a family of convergence curves is produced. Indeed, a similar pattern is observed for the other two eigenvalues shown in Figure 4, with each case showing a family of convergence curves for increasing p–refinement on each of the meshes.

Returning to the question of whether exponential convergence is in fact obtained. In the graphs of Figure 4 which show the logarithm of the relative error against $(\text{Ndof})^{1/2}$ we observe a similar pattern for each eigenvalue. The convergence with p–refinement on each of the meshes, produces a curve which approximately resembles a straight line until a precision of approximately 10^{-8} is reached. This value represents the finite precision of the method. Therefore, during the linear portion of the curve, the convergence of these eigenvalues can be regarded as exponential. The gradients of these lines becomes shallower as the number of elements in the mesh is increased. A similar behaviour has also been observed for smooth two–dimensional problems and so this behaviour should be expected for axisymmetric case also.

Next we consider the case with an angular wavenumber $m = 1$. The convergence of the first three eigenvalues, when computed on the sequence of quadrilateral meshes with polynomial orders $p = 0, 1, 2, 3, 4, 5$ in turn, is shown in Figure 5. These exhibit a similar convergence behaviour to that found for the case of $m = 0$.

The second set of results employ a discretisation consisting only of triangular elements. To obtain the triangular discretisation, each of the quadrilateral elements shown in the meshes given Figure 3 was subdivided in to two triangular elements. This resulted in a sequence of meshes with 2,8,32 and 128 triangular elements. On each of these meshes, the relative error of the first three eigenvalues was computed for angular wavenumber $m = 0$ using uniform polynomial orders of $p = 0, 1, 2, 3, 4, 5$ in turn. The resulting convergence curves are shown in Figure 6.

The convergence of the first three eigenvalues for angular wavenumber $m = 1$ for the triangular discretisation is shown in Figure 7.

5.2 Two concentric dielectric spheres

The next example we consider is that of two concentric dielectric spheres, of which an illustration can be found in Figure 8. For this example we assume that the radius of the first sphere is $a = 1$ and the radius of the second sphere is $b = 2$. The latter radii being a PEC boundary. The material properties of the inner sphere are $\epsilon_a = 10$, $\mu_a = 1$ and those of the outer sphere are $\epsilon_b = 1 = \mu_b = 1$. The exact eigenvalues for this problem may be computed, a description of which is given in [9].

A sequence of hybrid quadrilateral/triangular meshes were constructed to discretise this problem. The meshes contain 2 triangles and 2 quadrilaterals, 4 triangles and 12 quadrilaterals, 6 triangles and 30 quadrilaterals and 8 triangles and 56 quadrilaterals, respectively. An illustration of the hybrid meshes is given in Figure 9. To obtain the representation of the curved boundaries on these relatively coarse meshes, a blending function approach was implemented [31, 18]. Using this approach, allows us to align the edges of the elements with the true geometry of the problem.

Uniform polynomial orders of $p = 0, 1, 2, 3, 4, 5$ were considered, in turn, on each of the four hybrid meshes. The convergence of the relative errors for the first three eigenvalues for angular wavenumber $m = 0$ is shown in Figure 10. In this figure, we observe that, even on the coarsest mesh, relative errors of the order of 10^{-8} are obtained for the eigenvalues when p–refinement is performed. This indicates that the blending function approach combined with a high p is capable of accurately resolving the eigenmodes on very coarse meshes for cases when the boundary is curved

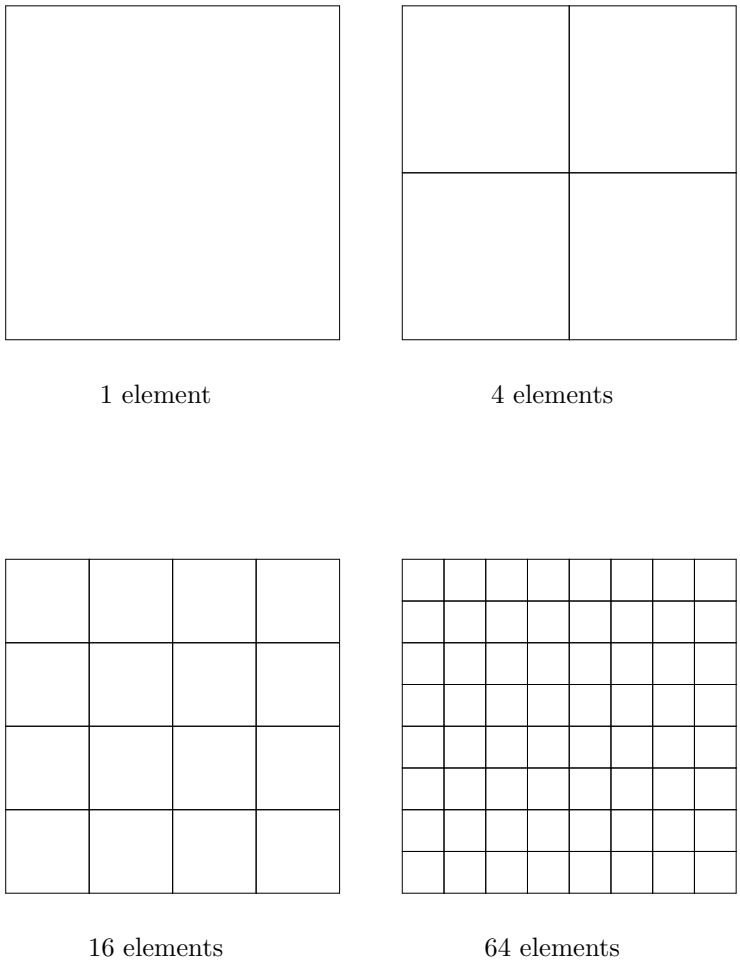

Figure 3: Axisymmetric eigenvalue calculations for a hollow cylindrical cavity of unit height and radius showing, a sequence of four quadrilateral meshes with uniform h–refinement

and when discontinuous material coefficients are employed. Families of similar curves are obtained when the finer meshes are employed.

When the relative error is plotted with respect to $\text{Ndof}^{1/2}$ the curves obtained resemble straight line plots until the precision limit is reached, thus indicating that the convergence of the eigenvalues is exponential for p–refinement. The gradients of these lines decreases as the number of elements in the mesh is increased in a similar manner to that already found for the case of the hollow cylindrical cavity.

5.3 Dielectric sphere in free space

We now consider the example of a dielectric sphere situated in free space. The radius of the sphere is $a = 1$ and its material properties are $\epsilon = 10$, $\mu = 1$. As the sphere is situated in free space, one must also include this region in the simulation. In this work, this achieved approximately through the truncation of the otherwise infinite domain and the application of absorbing sponge layer to the truncated domain. An illustration of the resulting configuration is given in Figure 11. We adopt a PML which has been derived in cylindrical coordinates [15]. The material tensors in the

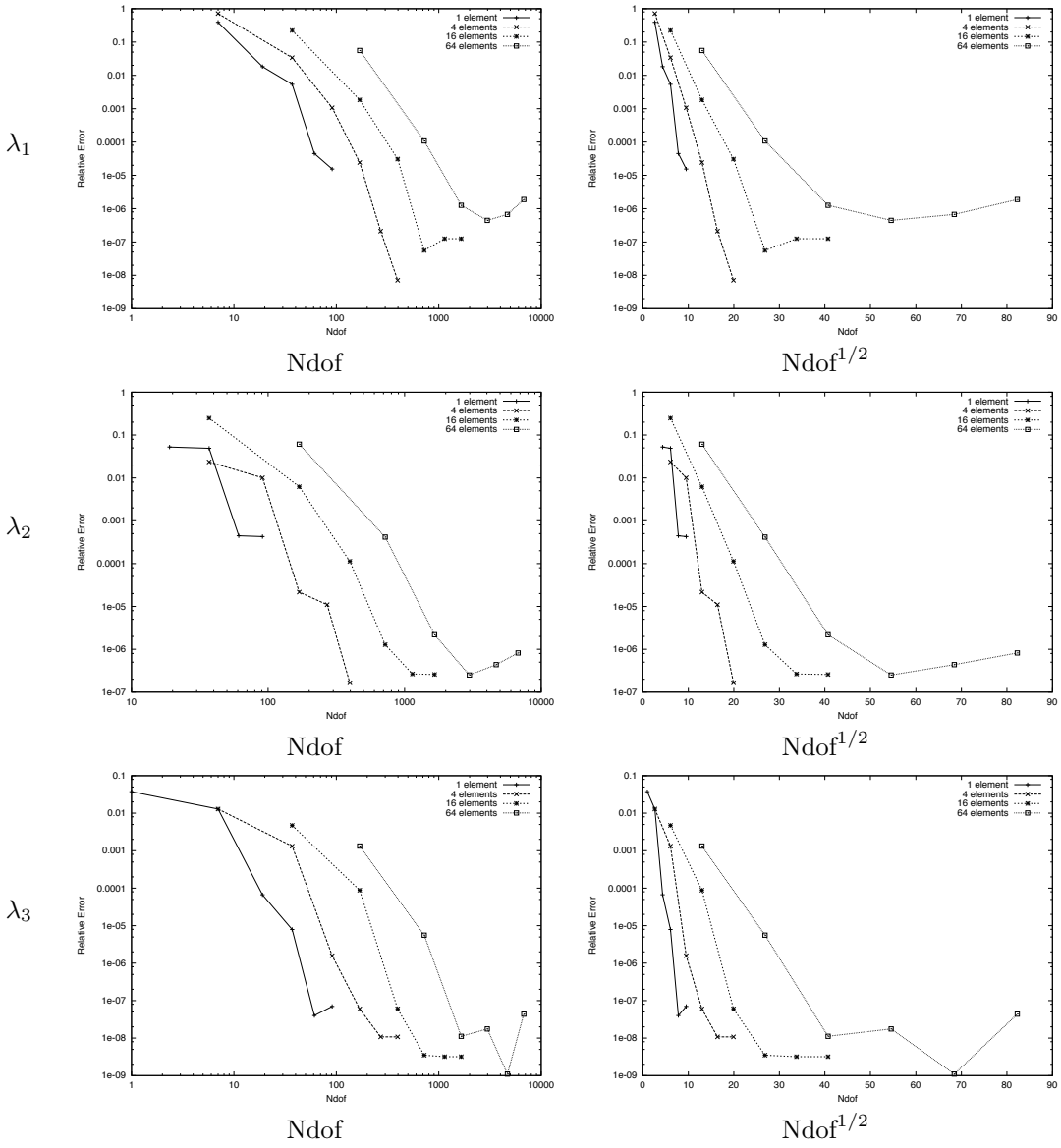

Figure 4: Axisymmetric eigenvalue calculations for a hollow cylindrical cavity of unit height and radius showing, the convergence of the relative error against Ndof and $(\text{Ndof})^{1/2}$ for the first three eigenvalues of angular wavenumber $m = 0$ on a sequence of quadrilateral meshes with uniform polynomial orders $p = 0, 1, 2, 3, 4, 5$ in turn.

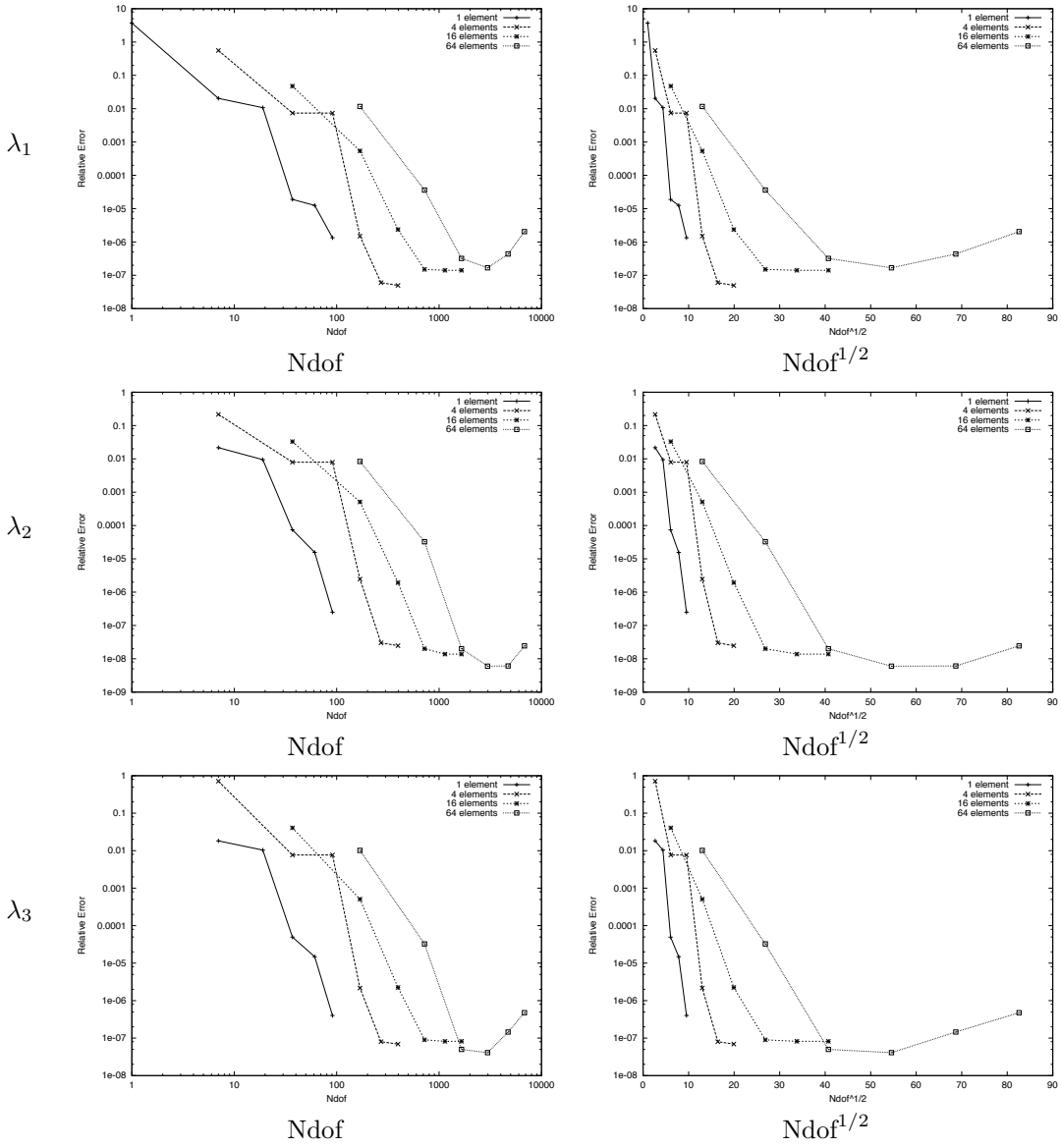

Figure 5: Axisymmetric eigenvalue calculations for a hollow cylindrical cavity of unit height and radius showing, the convergence of the relative error against Ndof and $(\text{Ndof})^{1/2}$ for the first three eigenvalues of angular wavenumber $m = 1$ on a sequence of quadrilateral meshes with uniform polynomial orders $p = 0, 1, 2, 3, 4, 5$ in turn.

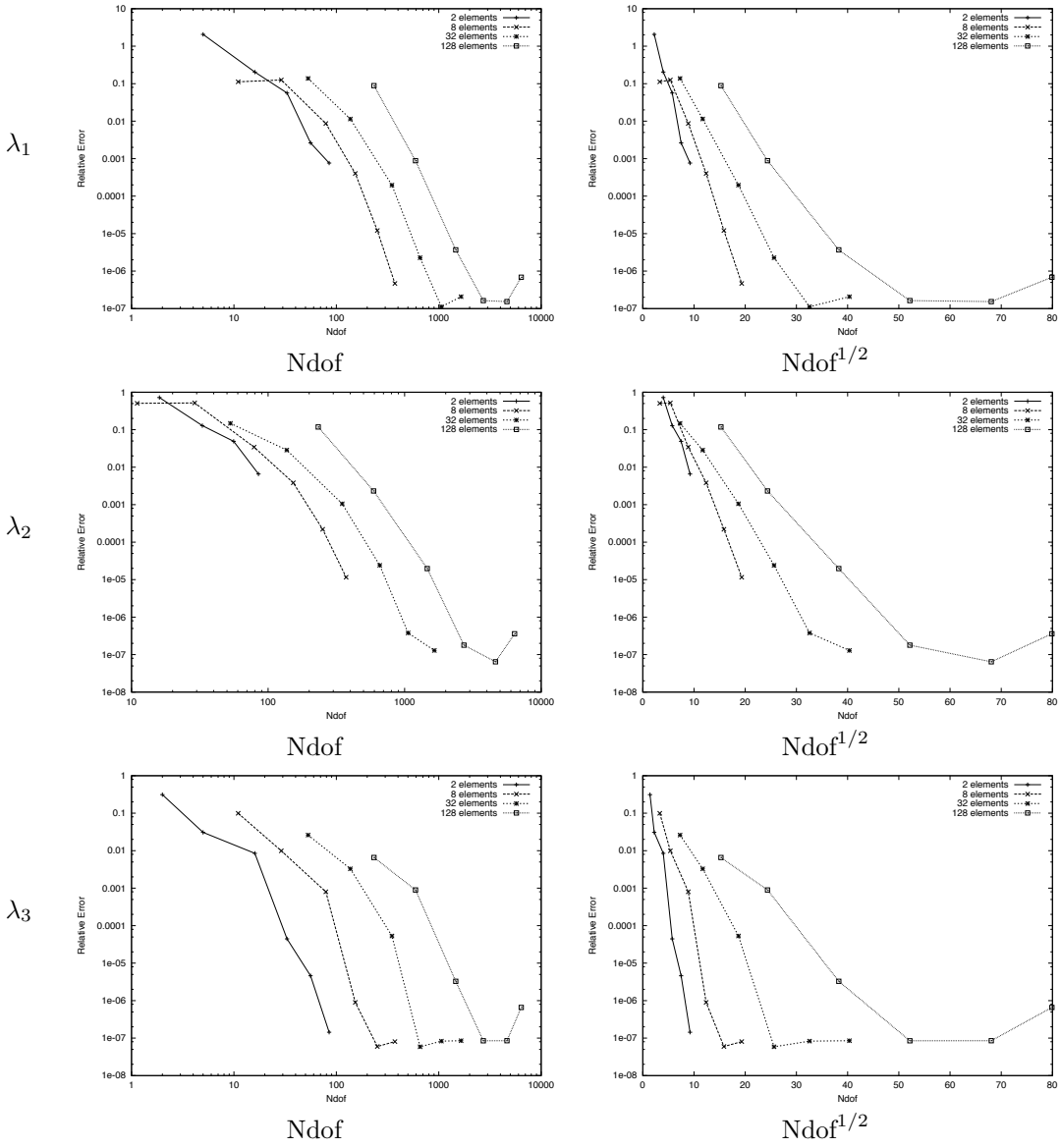

Figure 6: Axisymmetric eigenvalue calculations for a hollow cylindrical cavity of unit height and radius showing, the convergence of the relative error against Ndof and $(\text{Ndof})^{1/2}$ for the first three eigenvalues of angular wavenumber $m = 0$ on a sequence of triangular meshes with uniform polynomial orders $p = 0, 1, 2, 3, 4, 5$ in turn.

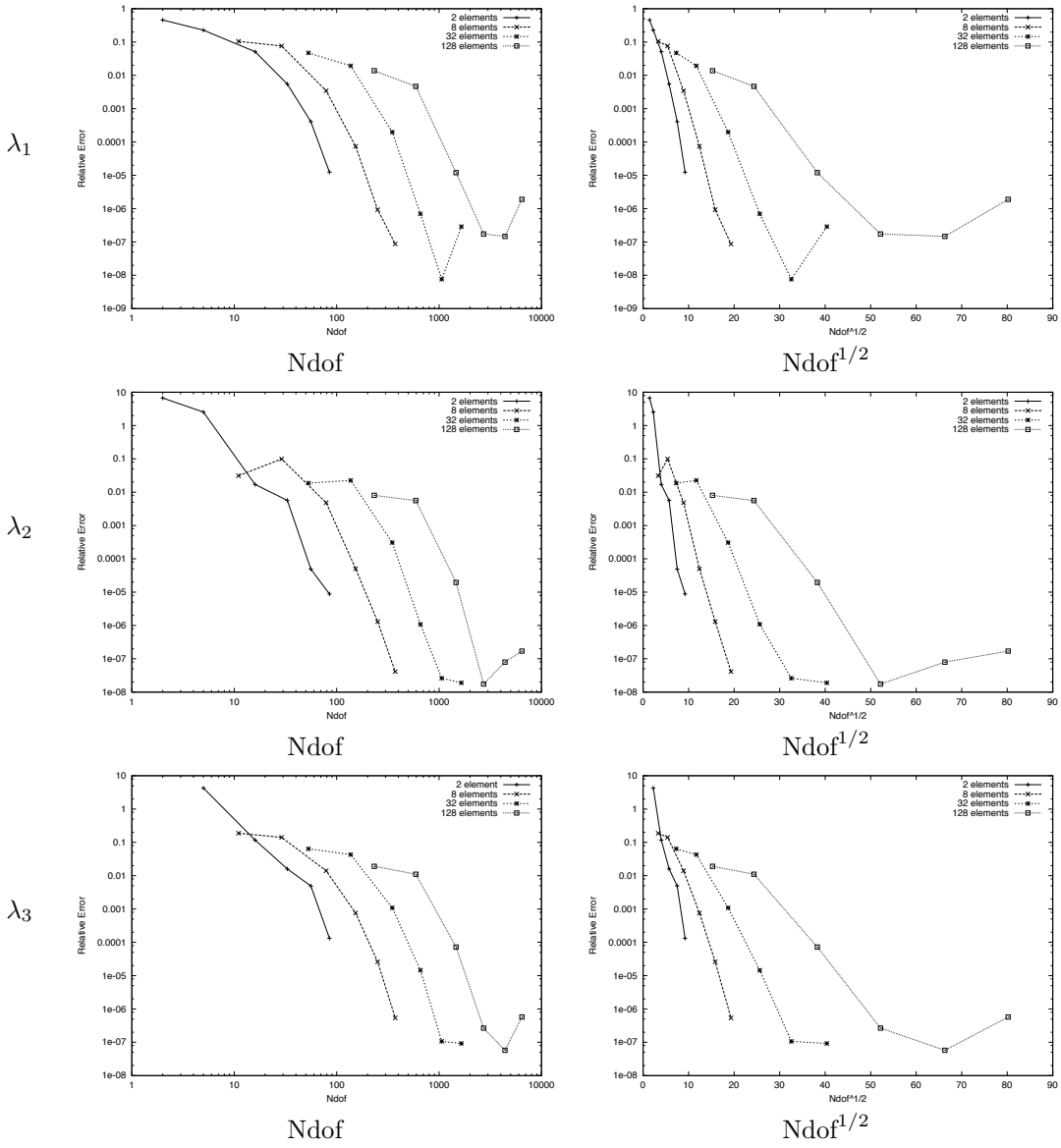

Figure 7: Axisymmetric eigenvalue calculations for a hollow cylindrical cavity of unit height and radius showing, the convergence of the relative error against Ndof and $(\text{Ndof})^{1/2}$ for the first three eigenvalues of angular wavenumber $m = 1$ on a sequence of triangular meshes with uniform polynomial orders $p = 0, 1, 2, 3, 4, 5$ in turn.

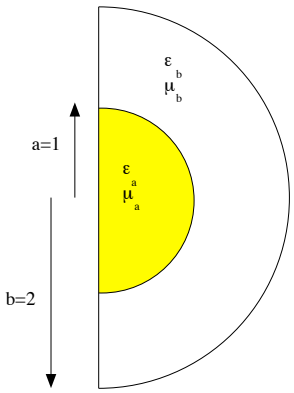

Figure 8: Axisymmetric eigenvalue calculation for an example containing two dielectric spheres of radii $a = 1$ and $b = 2$ respectively, showing the geometry of the problem

absorbing layer take the form

$$\epsilon = \mu = \Lambda = \begin{bmatrix} \Lambda_r & 0 & 0 \\ 0 & \Lambda_\theta & 0 \\ 0 & 0 & \Lambda_z \end{bmatrix} \tag{17}$$

With the specific complex-valued entries of the tensor being given in [15]. Note that $\Lambda_r, \Lambda_\theta$ and Λ_z are not constant, but a quadratic function of distance through the PML. A good choice of thickness and absorption parameter is proposed by Cohen [10]. He suggests adopting a PML of unit thickness together with a value $\sigma = 6$, and we adopt these choices for the simulations presented here.

Due to the material parameters being complex, the solution of the problem becomes inherently more computationally expensive. For this reason we report results for only a single mesh for this case and this is shown in Figure 12. In Figure 13, we report the relative error for the real and imaginary parts of the first eigenvalue for an angular wavenumber of $m = 1$ when uniform polynomial orders $p = 0, 1, 2, 3, 4, 5, 6$ are used in turn. We only show convergence of the relative error with respect to Ndof, as it obvious that, in this case, the convergence stagnates before exponential convergence can occur. The stagnation observed, occurs due to the approximate nature of the PML and manifests itself in both the real and imaginary parts of the first eigenvalue.

For greater levels of accuracy, one could attempt to design a better PML or use an alternative far field condition. Although neither option is easily accomplished as the research in to absorbing boundary conditions for open cavity problems is in its infancy.

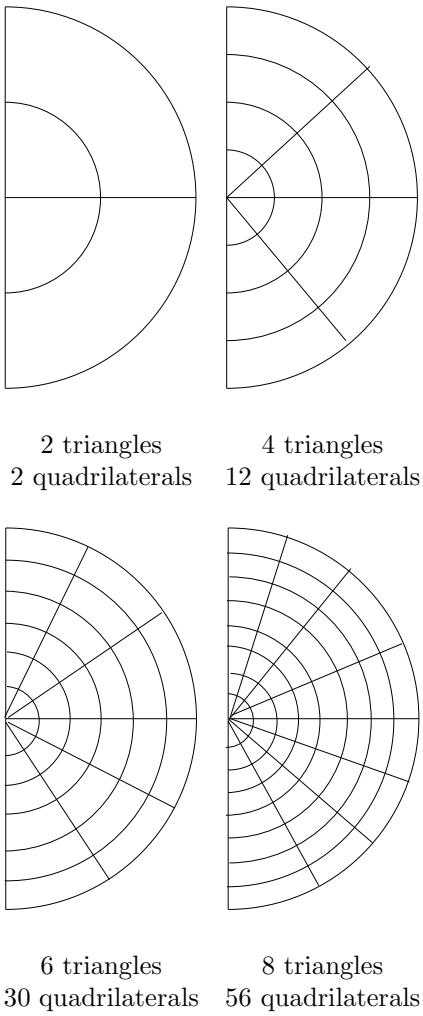

Figure 9: Axisymmetric eigenvalue calculations for an example containing two concentric dielectric spheres of radii $a = 1$ and $b = 2$ respectively showing, a sequence of four hybrid quadrilateral/triangular meshes with uniform h–refinement

6 Conclusions

This paper has shown an approach to solving axisymmetric eigenvalues which employs the hp finite element discretisation of Ainsworth and Coyle [2]. For sequence of closed cavities, exponential convergence of the eigenvalues has been demonstrated for quadrilateral, triangular and hybrid discretisations, both with straight and curved boundaries. The solution of open cavities was also shown to be possible with the approach, although a better far field condition is required to obtain higher levels of accuracy. This remains an area of on–going research.

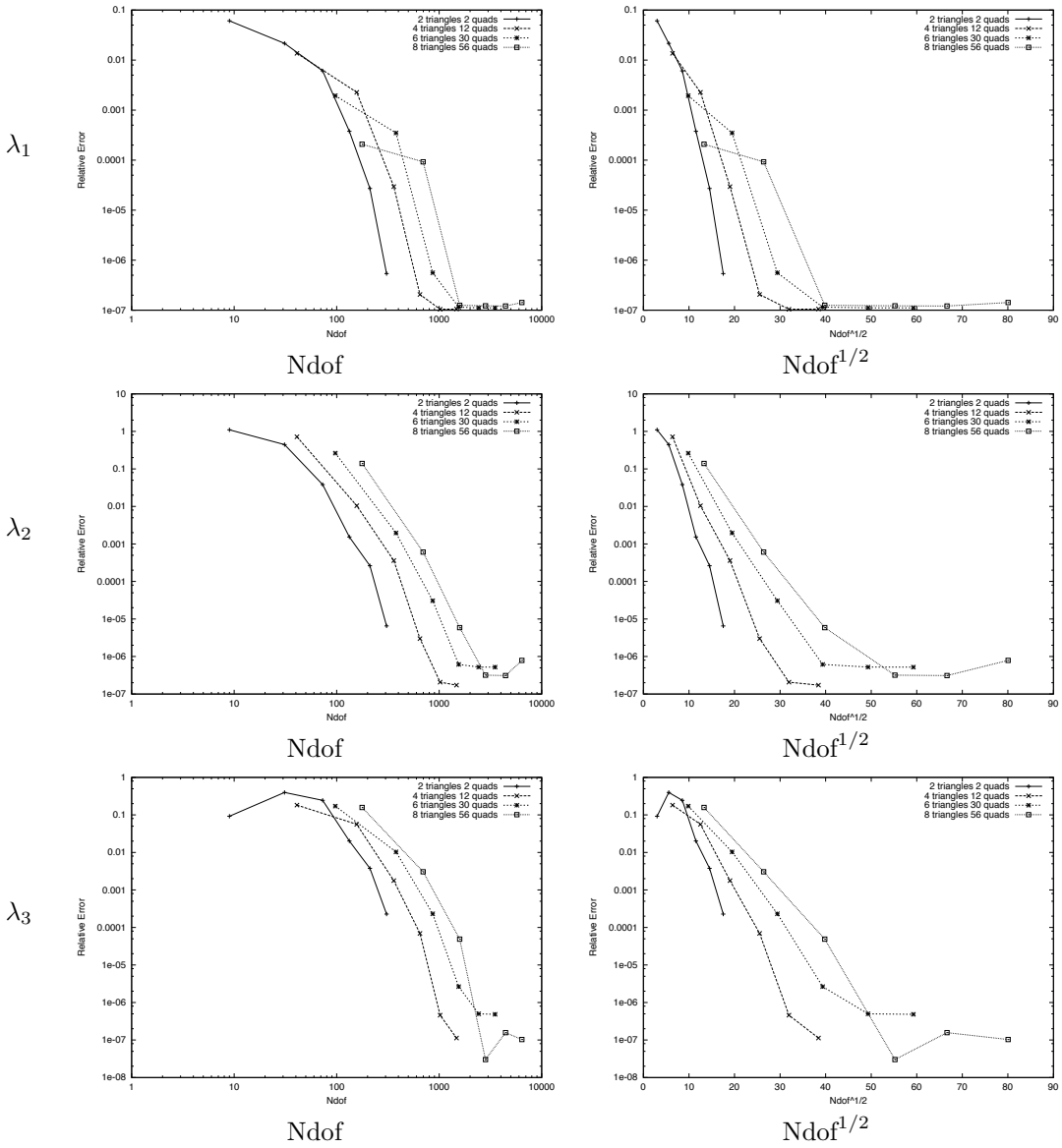

Figure 10: Axisymmetric eigenvalue calculations for an example containing two concentric dielectric spheres of radii $a = 1$ and $b = 2$ respectively showing, the convergence of the relative error against Ndof and $(\text{Ndof})^{1/2}$ for the first three eigenvalues of angular wavenumber $m = 0$ on a sequence of hybrid quadrilateral/triangular meshes with uniform polynomial orders $p = 0, 1, 2, 3, 4, 5$ in turn.

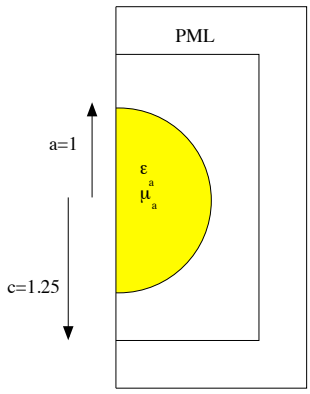

Figure 11: Axisymmetric eigenvalue calculation for an example containing a dielectric sphere of radius $a = 1$ located in free space, truncated with a PML at a distance of $c = 1.25$, showing the geometry of the problem

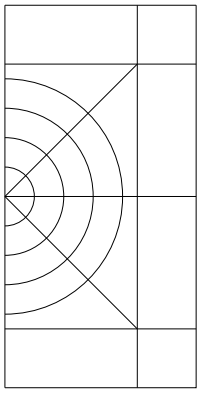

Figure 12: Axisymmetric eigenvalue calculation for an example containing a dielectric sphere of radius $a = 1$ located in free space, truncated with a PML at a distance of $c = 1.25$, showing the mesh of 22 quadrilaterals and 4 triangles

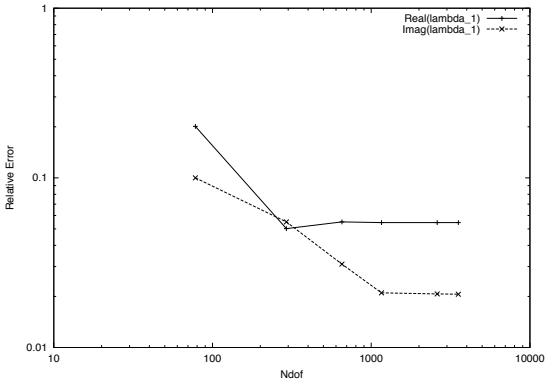

Figure 13: Axisymmetric eigenvalue calculation for an example containing a dielectric sphere of radius $a = 1$ located in free space, truncated with a PML at a distance of $c = 1.25$, showing the convergence of the relative error against Ndof for the first eigenvalue for an angular wavenumber $m = 1$ on a hybrid quadrilateral/triangular mesh with uniform polynomial orders $p = 0, 1, 2, 3, 4, 5, 6$ in turn.

References

[1] M. Ainsworth and J. Coyle. Computation of Maxwell eigenvalues on curvilinear domains using *hp*-version Nédélec elements. In *Proceedings of ENUMATH*, 2001.

[2] M. Ainsworth and J. Coyle. Hierarchic *hp*–edge element families for Maxwell's equations on hybrid quadrilateral/triangular meshes. *Computer Methods in Applied Mechanics in Engineering*, 190:6709–6733, 2001.

[3] M. Ainsworth and J. Coyle. Hierarchic finite element basses on unstructured tetrahedral meshes. Technical report, Department of Mathematics, University of Strathclyde, Glasgow, 2002.

[4] M. Ainsworth, J. Coyle, P.D. Ledger, and K. Morgan. Computation of Maxwell eigenvalues using higher order edge elements in three–dimensions. *IEEE Transactions on Magnetics*, 2002. Accepted.

[5] M. Ainsworth and K. Pinchedez. *hp*–Approximations theory for BDFM/RT finite elements and applications. *SIAM Journal on Numerical Analysis*, 2002. Accepted.

[6] L.S. Anderson and J.L. Volakis. Hierarchical tangential vector finite elements for tetrahedra. *IEEE Microwave and Guided Wave letters*, 8:127–129, 1998.

[7] J-P Berenger. A perfectly matched layer for the absorption of electromagnetic waves. *Journal of Computational Physics*, 114:185–200, 1994.

[8] O. Chinellato. *In preperation.* PhD thesis, Institute of Scientific Computing, ETH Zürich Switzerland, 2003.

[9] O. Chinellato, P. Abenz, M. Streiff, and A. Witzig. Computation of optical modes inside axisymmetric open cavity resonators. *Future Generation Computing Systems*, 2003. submitted.

[10] G.C. Cohen. *Higher Order Numerical Methods for Transient Wave Eqautions.* Springer, 2002.

[11] J. Coyle and P.D. Ledger. Evidence of exponential connvergence in the computation of Maxwell eigenvalues. *Computer Methods in Applied Mechanics*, 2003. Submitted.

[12] L. Demkowicz and W. Rachowicz. A 2d *hp* adaptive finite element package for electromagnetics. Technical report, TICAM Report 98-15, University of Texas at Austin.

[13] L. Demkowicz and L. Vardapetyan. Modeling of electromagnetic/scattering problems using *hp*–adaptive finite elements. *Computer Methods in Applied Mechanics and Engineering*, 152:103–124, 1998.

[14] R.D. Graglia, D.R. Wilton, and A.F. Peterson. Higher order interpolatory vector bases for computational electromagnetics. *IEEE Transactions on Antennas and Propagation*, 45:329–341, 1997.

[15] A.D. Greenwood and J.-M. Jin. Finite element analysis of complex axisymmetric radiating structures. *IEEE Antennas and Propagation Society*, 1:476–479, 1999.

[16] Y. Iwashita. Accuracy of eigenvalues obtained with hybrid elements on axisymmetirc domains. *IEEE Transactions on Magnetics*, pages 2543–2546, 1998.

[17] A. Kamerai. Symmetric second order edge elements for triangles and tetrahedra. *IEEE Transactions on Magnetics*, 35:1394–1397, 1999.

[18] P.D. Ledger. *An hp-Adaptive Finite Element Proceedure for Electromagnetic Scattering Problems.* PhD thesis, Dept. Civil Engineering, University of Wales, Swansea, 2002.

[19] P.D. Ledger, K. Morgan, O. Hasan, and N.P. Weatherill. Arbitrary order edge elements for electromagnetic scattering simulations usung hybrid meshes and a pml. *International Journal for Numerical Methods in Engineeing*, 55:339–358, 2002.

[20] J.-F. Lee, G.M. Wilkins, and R. Mittra. Finite element analysis of axisymmetric cavity resonator using a hybrid edge element technique. *IEEE Transactions on Microwave Theory and Techniques*, 41:1981–1987, 1993.

[21] G. Mur. Edge elements, their advantages and their disadvantages. *IEEE Transactions on Magnetics*, 30:3552–3557, 1994.

[22] J.C. Nédélec. Computation of eddy currents on a surface in $\mathbb{R}^3$ by finite element methods. *SIAM Journal of Numerical Analysis*, 15:580–594, 1978.

[23] J.C. Nédélec. Mixed elements in $\mathbb{R}^3$. *Numerische Mathematik*, 35:315–341, 1980.

[24] J.C. Nédélec. A new family of mixed elements in $\mathbb{R}^3$. *Numerische Mathematik*, 50:57–81, 1986.

[25] M.J. Noble, J.A. Lott, and J.P. Loehr. Quasi–exact optical analysis of oxide-apertured microcavity VCSL's using vector finite elements. *IEEE Journal of Quantum Electronics*, 34:2337–2339, 1998.

[26] W. Rachowicz and L. Demkowicz. A three dimensional *hp*–adaptive finite element package for electromagnetics. *International Journal for Numerical Methods in Engineering*, 53:147–180, 2002.

[27] A.J. Ruiz-Genovés, L.E. García-Castillo, and M. Salazar-Palma. Third–order Nédélec tetrahedral finite element. In *Proceedings of ECCOMAS Computational Fluid Dynamics Conference, Swansea WALES*, 2001.

[28] M. Streiff, A. Witzig, and W. Fichtner. Computing optical modes for vcsel device simulation. *IEE Proc. Optoelectron*, 149, 2002.

[29] A.H. Stroud and D. Secrest. *Guassian Quadrature Formulas*. Englewood Cliffs NJ, 1966.

[30] D. Sun, J. Manges, X. Yuan, and Z. Cendes. Spurious modes in finite-element methods. *IEEE Antennas and Propagation Magazine*, 37:12–24, 1995.

[31] B. Szabo and I. Babuska. *Finite Element Analysis*. John Wiley and Sons, 1991.

[32] J.P. Webb. Hierarchical vector basis functions of arbitrary order for triangular and tetrahedral finite elements. *IEEE Transactions on Antennas and Propagation*, 47:1244–1253, 1999.

[33] M.F. Wong, M. Prak, and V.F. Hanna. Axisymmetric edge based finite formulation for bodies of revolution: application to dielectric resonators. *IEEE Microwave Symposium Digest*, 1:285–288, 1995.

Research Reports

No.	Authors	Title
03-15	R. Hiptmair, P.E. Ledger	Computation of Resonant Modes for Axisymmetric Cavities using *hp*-Version Finite Elements
03-14	V.H. Hoang, C. Schwab	High-dimensional finite elements for elliptic problems with multiple scales
03-13	A. Toselli, X. Vasseur	A numerical study on Neumann-Neumann methods for *hp* approximations on geometrically refined boundary layer meshes II: Three-dimensional problems
03-12	X. Feng, M. von Oehsen, A. Prohl	Rate of Convergence of Regularization Procedures and Finite Element Approximations for the Total Variation Flow
03-11	P.-A. Nitsche	Best N Term Approximation Spaces for Sparse Grids
03-10	J.T. Becerra Sagredo	Z-splines: Moment Conserving Cardinal Spline Interpolation of Compact Support for Arbitrarily Spaced Data
03-09	P. Houston, D. Schötzau, Th. Wihler	Energy norm a-posteriori error estimation for mixed discontinuous Galerkin approximations of the Stokes problem
03-08	R. Hiptmair, A. Buffa	Coercive combined field integral equations
03-07	R. Hiptmair, O. Sterz	Current and Voltage Excitations for the Eddy Current Model
03-06	A.-M. Matache, P.-A. Nitsche, C. Schwab	Wavelet Galerkin Pricing of American Options on Lévy Driven Assets
03-05	M. Becheanu, R.A. Todor	On the Set of Diameters of Finite Point-Sets in the Plane
03-04	C. Schwab, R.A. Todor	Sparse finite elements for stochastic elliptic problems - higher order moments
03-03	R. Sperb	Bounds for the first eigenvalue of the elastically supported membrane on convex domains
03-02	F.M. Buchmann	Computing exit times with the Euler scheme
03-01	A. Toselli, X. Vasseur	Domain decomposition preconditioners of Neumann-Neumann type for *hp*-approximations on boundary layer meshes in three dimensions
02-26	M. Savelieva	Theoretical study of axisymmetrical triple flame
02-25	D. Schötzau, C. Schwab, A. Toselli	Mixed *hp*-DGFEM for incompressible flows III: Pressure stabilization